Journal of Power Sources 222 (2013) 326–332

Contents lists available at SciVerse ScienceDirect

Journal of Power Sources

journal homepage: www.elsevier.com/locate/jpowsour

A composite electrode consisting of nickel hydroxide, carbon nanotubes, and reduced graphene oxide with an ultrahigh electrocapacitance

Li Li Zhang [a], Zhigang Xiong [b], X.S. Zhao [b,*]

[a] Department of Chemical and Biomolecular Engineering, National University of Singapore, 4 Engineering Drive 4, Singapore 117576, Singapore
[b] School of Chemical Engineering, The University of Queensland, St Lucia Campus, St Lucia, QLD 4072, Australia

HIGHLIGHTS

- ► $Ni(OH)_2$ embedded in carbon nanotubes as pillars for graphene sheets was prepared.
- ► The composite showed a high specific capacitance and good cycle stability.
- ► High performance is due to the unique 3D nanostructure of the capacitor electrode.

GRAPHICAL ABSTRACT

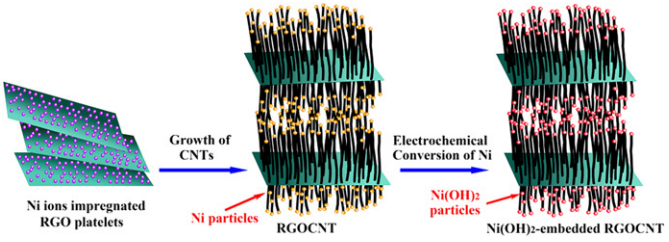

ARTICLE INFO

Article history:
Received 28 May 2012
Received in revised form
4 September 2012
Accepted 6 September 2012
Available online 15 September 2012

Keywords:
Nickel hydroxide
Carbon nanotubes
Reduced graphene oxide
Composite
Supercapacitor

ABSTRACT

A novel 3D nanostructure consisting of $Ni(OH)_2$ nanoparticles, carbon nanotubes (CNTs), and reduced graphene oxide with an extremely high electrocapacitance is described. The nanostructure consists of CNTs with embedded $Ni(OH)_2$ nanoparticles as pillars for reduced graphene oxide sheets. Electrochemical results show that the composite displays specific capacitances as high as 1235 and 780 F g^{-1} at current densities of 1 and of 20 A g^{-1}, respectively. In addition, the composite retains 80% of its original capacity after 500 cycles at a discharge current density of 10 A g^{-1}. This 3D pseudocapacitor electrode has a number of important features, such as fast ion and electron transfer, easy access of pseudoactive species and efficient utilization, and excellent reversibility of $Ni(OH)_2$ nanoparticles.

1. Introduction

Nickel hydroxide, $Ni(OH)_2$, has been widely used as a positive electrode in commercial alkaline rechargeable batteries [1–3]. Recent research results have shown that it is also a promising candidate for pseudocapacitors owing to its well-defined electrochemical redox activity, high specific capacitance, low cost, and the availability of various morphologies [4–9]. The major issues associated with $Ni(OH)_2$ when used as an electrode are its poor electrical conductivity and volume expansion or swelling during charge/discharge cycles, especially for high-rate applications [10,11]. Therefore, considerable effort has been made to improve the electrochemical performance of $Ni(OH)_2$ by tuning its morphology at nanoscale [10,12–15] and modifying it to make composite materials [8,9,16–18]. The highest specific capacitance observed on a $Ni(OH)_2$-nickel foam composite is 3152 F g^{-1} at a current density of 4 A g^{-1} [9]. However, the composite displayed a significant capacitance loss – about 50% of initial capacitance loss after 300 cycles. In addition, the specific capacitance was dropped to 280 F g^{-1} at a current density of 16 A g^{-1}. Wang and co-workers [8,19] described a two-step method to grow $Ni(OH)_2$ nanocrystals

* Corresponding author. Tel.: +61 7 33469997; fax: +61 7 33654199.
E-mail address: george.zhao@uq.edu.au (X.S. Zhao).

0378-7753/$ – see front matter © 2012 Elsevier B.V. All rights reserved.
http://dx.doi.org/10.1016/j.jpowsour.2012.09.016

on graphene. The authors observed that highly crystalline $Ni(OH)_2$ nanoplates grown on high-quality graphene sheets possessed a specific capacitance of about 935 F g^{-1}.

Three-dimensional (3D) nanoporous structures have been shown to have advantages in many technological applications, such as hydrogen storage [20] and supercapacitors [21–23]. Recently, we have demonstrated an approach to the preparation of porous conducting-polymer-pillared graphene oxide (GO) and reduced graphene oxide (RGO) sheets [24,25]. We have also reported a method for the preparation of 3D porous carbon-nanotube-pillared GO and RGO nanostructures [26]. Excellent electrical conductivity, efficient electron transfer and high specific surface area were observed from the carbon-nanotube-pillared RGO composite.

On the basis of our previous studies [24–26], we here demonstrate an approach to preparing graphene-based composite materials consisting of RGO sheets, $Ni(OH)_2$ nanoparticles and carbon nanotubes (CNTs). The composite materials displayed an excellent electrochemical performance as a pseudocapacitor electrode with specific capacitances of 1235 F g^{-1} at a current density of 1 A g^{-1} and 780 F g^{-1} at a higher current density of 20 A g^{-1}, as well as a good cycle stability. The superior electrochemical performance of the composite materials is attributed to the desirable 3D conducting architecture and the well-defined redox properties of the $Ni(OH)_2$ nanoparticles. To the best of our knowledge, this is the first work demonstrating the preparation of 3D CNT-pillared RGO sheets with embedded $Ni(OH)_2$ nanoparticles for pseudocapacitors.

2. Experimental section

2.1. Preparation of GO and RGO

The GO dispersion was prepared by sonication of graphite oxide, which was prepared from natural graphite (crystalline graphite flakes, particle size ranging from 45 to 500 μm, carbon content was 99%) using a modified Hummers method [25,27]. 5 g of graphite and 2.5 g of $NaNO_3$ were mixed with 120 mL of H_2SO_4 (95 wt%) in a 500 mL flask. The mixture was stirred for 30 min in an ice bath. While maintaining vigorous stirring, 15 g of $KMnO_4$ was added. The rate of addition was carefully controlled to keep the reaction temperature below 20 °C. The ice bath was then removed and the mixture was stirred at room temperature for about 12 h. As the reaction progressed, the mixture gradually became pasty, and the color turned into light brownish. 150 mL of deionized (DI) water was slowly added to the mixture under vigorous agitation. The reaction temperature was rapidly increased to 98 °C with effervescence, and the color changed to yellow. After the diluted suspension was stirred for 24 h, 50 mL of 30% H_2O_2 was added. The mixture was washed with 5% HCl and then DI water for several times to obtain solid GO. Dispersion of the GO in water was conducted under sonication.

The reduction of GO was carried using the sodium borohydride reduction method [26]. 0.3 g of GO was dispersed in 100 mL of DI water. The GO solution was sonicated for about 20 min. 0.4 g of sodium borohydride was then added and the mixture was heated in an oil bath at 100 °C for 24 h. The final RGO sample was obtained after repeated washing with DI water followed by centrifugation.

2.2. Preparation of RGOCNTs

The RGOCNT nanocomposites were prepared using the CVD method [26]. 2 g of sodium dodecyl sulfate (SDS, Merck) was dissolved in 40 mL of DI water. 20 mL of RGO dispersion of concentration 5 mg mL^{-1} was added into the above solution. After the mixture was sonicated for about 20 min, 1.74 g of nickel nitrate hexahydrate ($Ni(NO_3)_2 \cdot 6H_2O$, Alfa Aesar) dissolved in 20 mL of DI water was added dropwise under vigorous stirring. The resulting mixture was diluted with DI water to have a total volume of 120 mL and heated to 90 °C under stirring. After 16 h, the mixture was evaporated and dried in air at 60 °C for 24 h to obtain Ni-loaded RGO platelets. The Ni/C ratio (mass ratio between $Ni(NO_3)_2 \cdot 6H_2O$ and RGO) was varied to be 0.6, 2 and 4 to change the loading of Ni catalyst. The amount of SDS was adjusted according to the amount of $Ni(NO_3)_2 \cdot 6H_2O$ added.

The growth of CNTs was conducted on the Ni-loaded RGO at 850 °C using the CVD method with acetonitrile as the carbon source as has been described previously [28]. The CVD deposition time was varied from 15 min to 30 min to control the length of the CNTs. The samples are denoted as RGOCNT-X-Y, where X stands for CVD time (15 or 30 min) while Y refers to the Ni catalyst loading expressed using Ni/C ratio. For examples, sample RGOCNT-15-4 was prepared using a Ni/RGO ratio of 4 and a CVD time of 15 min while GOCNT-30-2 was obtained from Ni/C ratio of 2 and CVD time of 30 min. For comparison purpose, GO was also used as substrate to prepare GOCNT-15-4 composite followed exactly the same procedure as that described for RGOCNT-15-4.

2.3. Characterization

The microscopic feature of the samples was observed on a FESEM (JSM 6700F, JEOL Japan) operated at 10 kV and a TEM (JEM 2010, JEOL, Japan) operated at 200 kV. The pore structure of the sample was investigated using physical adsorption of nitrogen at the liquid-nitrogen temperature (77 K) on an automatic volumetric sorption analyzer (NOVA1100, Quantachrome). Prior to measurement, a sample was vacuum-degassed at 200 °C for 5 h. The specific surface area (S_{BET}) was determined according to the Brunauer–Emmett–Teller (BET) method in the relative pressure range of 0.01–0.2. The total pore volume (V_t) was obtained from the volume of nitrogen adsorbed at a relative pressure of 0.99. X-ray diffraction (XRD) patterns were collected on an XRD-6000 (Shimadzu, Kyoto, Japan) with Cu Kα radiation ($\lambda = 1.5418$ Å) as the X-ray source. XPS analysis was carried out on an AXIS HSI 165 spectrometer (Kratos Analytical) using a monochromatized Al Kα X-ray source (1486.71 eV). The EIS was collected using an Autolab PGSTAT302N with amplitude of 10 mV in the frequency range from 100 kHz to 1 mHz at room temperature. The electrical conductivities were measured on pellets (13 mm in diameter, with top and bottom electrodes), which was prepared under a pressure of 500 kg at room temperature [29].

2.4. Measurement of electrochemical properties

A three-electrode cell system was used to evaluate the electrochemical performance using both the CV and galvanostatic charge–discharge techniques on an Autolab PGSTAT302N at room temperature. The working electrode was prepared by casting a nafion-impregnated sample onto a glassy carbon electrode with diameter of 5 mm [24,25]. Typically, 5 mg composite material was dispersed in 1 mL ethanol solution containing 5 μL nafion solution (5 wt% in water) by sonication for 20 min. This sample (40 μL) was then dropped onto the glassy carbon electrode and dried in an oven before the electrochemical test. The mass loading of the sample on the glassy carbon electrode is 1 mg cm^{-2}.

Prior to the electrocapacitive measurements, all the RGOCNT and GOCNT composite electrodes were subjected to the cyclic

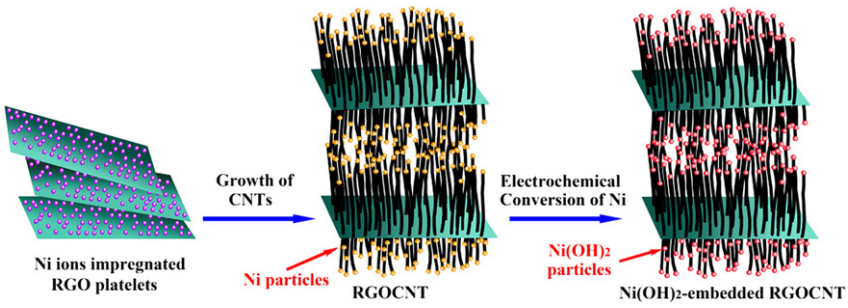

Scheme 1. Schematic illustration of the experimental steps for the preparation of $Ni(OH)_2$ embedded-carbon-nanotube-graphene composite.

voltammetry sweep at the scan rate of 5 mV s^{-1} in the potential range of −1.0 V–0.1 V to electrochemically convert the nickel nanoparticles to nickel hydroxides in a 6 M KOH electrolyte solution. Afterward, the electrochemical properties of the sample were evaluated in the potential range of −0.1 V–0.4 V. The specific gravimetric capacitance (C in F g^{-1}) was obtained from the discharge curve according to the following equation [30,31]:

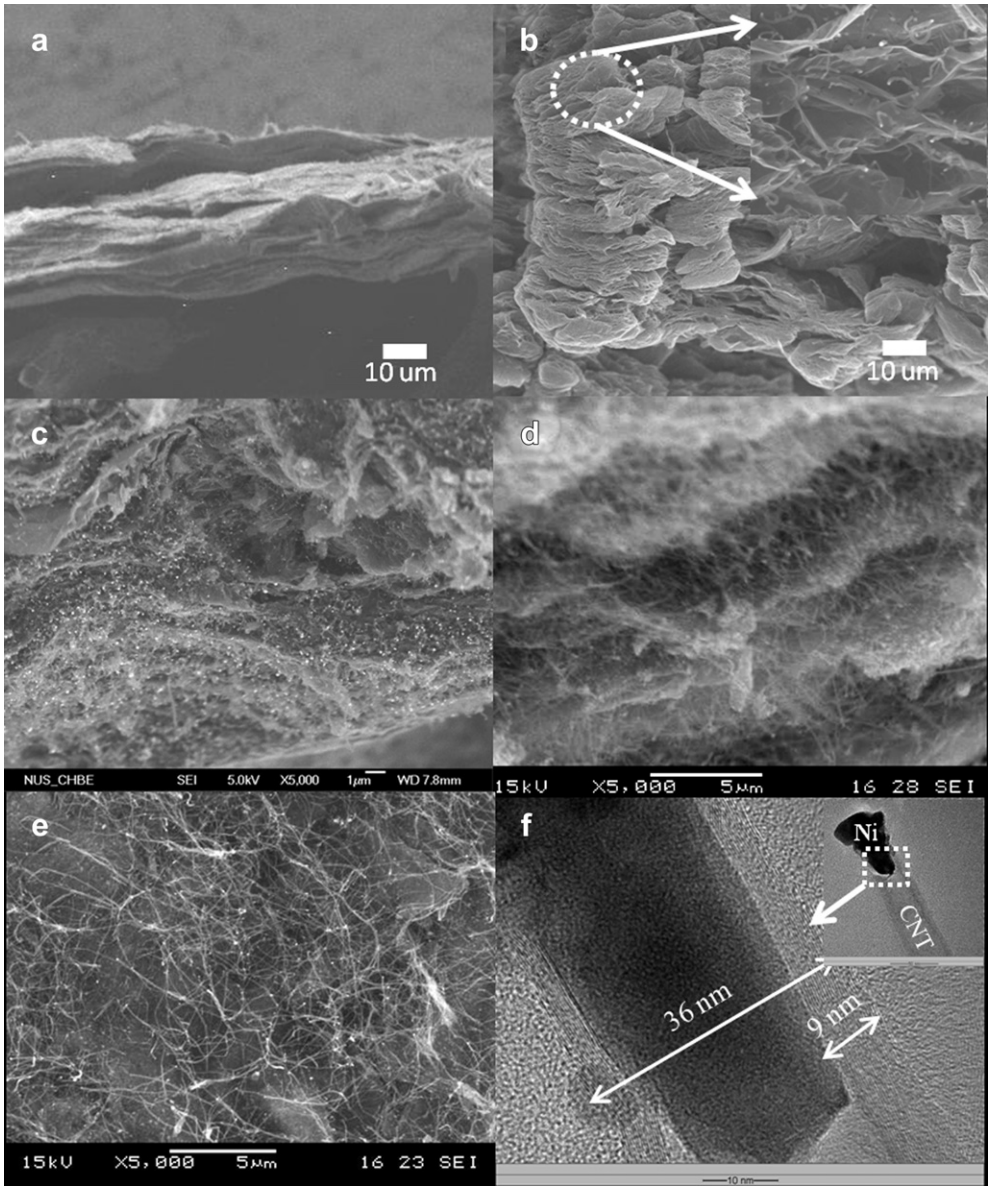

Fig. 1. FESEM images of (a) restacked RGO platelets after impregnation with nickel nitrate, (b) RGOCNT composite after CVD of 15 min, (c) sample RGOCNT-15-0.6, (d) sample RGOCNT-15-4, and (e) sample RGOCNT-30-2. (f) TEM image of sample RGOCNT-15-4.

$$C = \frac{I\Delta t}{\Delta V \times m} \quad (1)$$

where I is the current loaded (A), Δt is the discharge time (s), ΔV is the potential change during discharge, and m is the mass of active material in a single electrode (g).

3. Results and discussion

The experimental steps for the preparation of samples are illustrated in Scheme 1. The details for the preparation of CNT-pillared RGO (RGOCNT) can be found elsewhere [26]. The $Ni(OH)_2$-embedded RGOCNT was obtained through electrochemical conversion of the nickel nanoparticles in an alkaline solution using the cyclic voltammetry technique (see details in the experimental section). Fig. 1a shows the scanning electron microscopy (SEM) image of the restacked RGO platelets after impregnation with nickel. A layered RGO structure can be clearly seen. After the growth of CNTs using the chemical vapor deposition (CVD) method with acetonitrile as the carbon source for 15 min, the layered structure was well maintained, but with a significant volume expansion as can be seen from Fig. 1b. The magnified field-emission scanning electron microscopy (FESEM) image shown in the inset of Fig. 1b clearly reveals the growth of CNTs between RGO platelets. The growth of the CNT pillars can be controlled by the loading amount of nickel catalyst and the CVD time [26]. Fig. 1c,d show the FESEM images of various CNT-pillared RGO composites with different amounts and lengths of CNTs. Samples RGOCNT-15-0.6 and RGOCNT-15-4 prepared with a shorter CVD time (Fig. 1c,d) displayed a layered structure with short CNTs between the RGO platelets. Increasing the CVD time from 15 min to 30 min resulted in CNT pillars of long length. It is also seen that CNTs covered the external surface of sample RGOCNT-30-2 (Fig. 1e). The detailed structure of the CNT pillars in sample RGOCNT-15-4 can be seen from the transmission electron microscopy (TEM) image in Fig. 1f. The inset in Fig. 1f revealed that the nickel catalyst particles resided at the top of the CNT, implying a tip growth mechanism for the CNTs [32]. A high-magnification TEM image showed that the graphitic multi-layered walls of CNT aligned parallel to the tube axis. The wall thickness and the diameter of the CNT were about 9 and 36 nm, respectively. A careful observation of the TEM image showed that one nickel catalyst particle was half-embedded in the tip of each CNT with another half of the catalyst particle exposing to the surrounding environment. This is very important as such a Ni structure would allow not only a strong interaction between the particle and the CNT, but also make it available for subsequent electrochemical reactions.

The electrochemical conversion of metallic nickel to nickel hydroxide in an alkaline solution has been decomented [3,33,34]. In this work, we used the cyclic voltammetry (CV) method to convert the nickel nanoparticles to $Ni(OH)_2$ in order to utilize its highly reversible redox property in an alkaline electrolyte. As can be seen from Fig. S1, in the potential range of −1.0–0.1 V, irreversible chemical reactions occurred as evidenced by the single anodic current peak in the first cyclic voltammetry cycle. This peak corresponds to the reaction of nickel particles in the alkaline solution ($Ni + 2OH^{-1} = Ni(OH)_2 + 2e^{-1}$) [34]. In the following cycles in the same potential range, the CV curves showed a fairly rectangular shape, which is typical for an electrical double layer capacitance.

X-ray photoelectron spectroscopy (XPS) was used to analyze the nickel composition before and after the electrochemical conversion for sample RGOCNT-15-4. The Ni $2p_{3/2}$ core-level XPS spectrum (Fig. 2) showed one sharp peak centered at 852.7 eV, corresponding to the metallic state of nickel [35]. After the electrochemical conversion, the Ni $2p_{3/2}$ peak shifted to a higher binding energy at 855.8 eV, which is corresponding to nickel hydroxide [17]. Fig. S2 shows the X-ray diffraction (XRD) patterns of the RGOCNT sample before and after electrochemical conversion (EC). The presence of pure metallic Ni on the sample before EC can be clearly seen (JCPDS No. 04-850). After EC, the characteristic peaks of metallic Ni disappeared while small peaks at 33.1, 38.4 and 52.1 degrees two theta appeared. These peaks are attributed to $Ni(OH)_2$ [8]. Both the XPS and XRD results confirmed the conversion of metallic nickel particles to nickel hydroxide during the EC reaction.

The electrochemical properties of the $Ni(OH)_2$-embedded-RGOCNT-15-4 composite were evaluated and the results are shown in Fig. 3. From the CV curves of sample RGOCNT-15-4 measured in the potential range of −0.1–0.4 V at various scan rates (Fig. 3a), a pair of very strong redox current peaks can be seen. This is due to the reversible reaction between Ni (II) and Ni (III) [8–10,17]. It is seen from Fig. 3b that there is only one anodic (oxidation) peak and one cathodic (reduction) peak on the CV curve. The difference between the anodic and cathodic peaks is about 100 mV. The difference ΔE_{OR} (E_O–E_R) between the oxidation potential and the reduction potential can be taken as a measure of the reversibility of the electrode reaction [10,36]. The smaller the value of ΔE_O is, the higher reversibility of the reaction is. Comparing the ΔE_{OR} value observed in this work with those reported in the literature (e.g., 120 mV for tubular $Ni(OH)_2$ and 180 mV for spherical powder) [10], the smaller ΔE_{OR} observed in this work indicated a good reversibility of the electrochemical redox reaction for the composite electrode. In addition, the difference between the oxygen evolution potential (E_{OE}) and E_O is another important indicator for raising the oxygen evolution overpotential [17,37]. The larger the value is, the better the charge efficiency of the active material is. That is, a large difference between E_{OE} and E_O allows fully oxidation of Ni (II) to Ni (III) before the evolution of the oxygen. The potential difference (E_{OE}–E_O) was 130 mV for the present electrode, higher than that reported in the literature [10,17]. Thus, composite material RGOCNT-15-4 is an excellent pseudocapacitive electrode material.

Fig. 3c shows the galvanostatic charge–discharge curves at various discharge current densities ranging from 1 to 20 A g^{-1}. It was calculated that the specific capacitance was as high as 1235 F g^{-1} at the discharge rate of 1 A g^{-1} based on the total

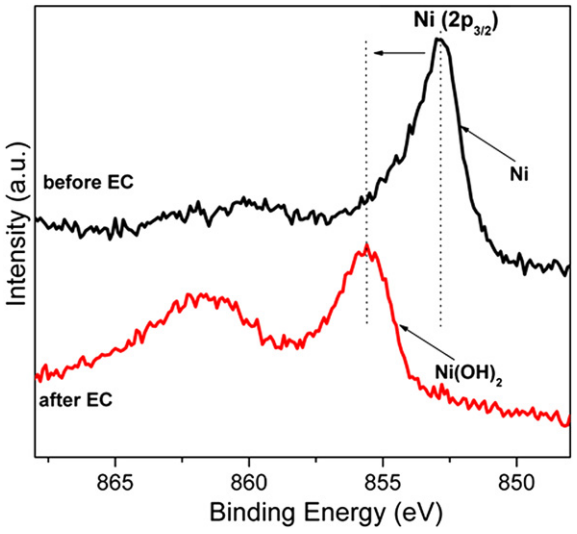

Fig. 2. Ni 2p3/2 core-level XPS spectra of sample RGOCNT-15-4 before and after electrochemical conversion using the cyclic voltammetry method in a 6 M KOH electrolyte.

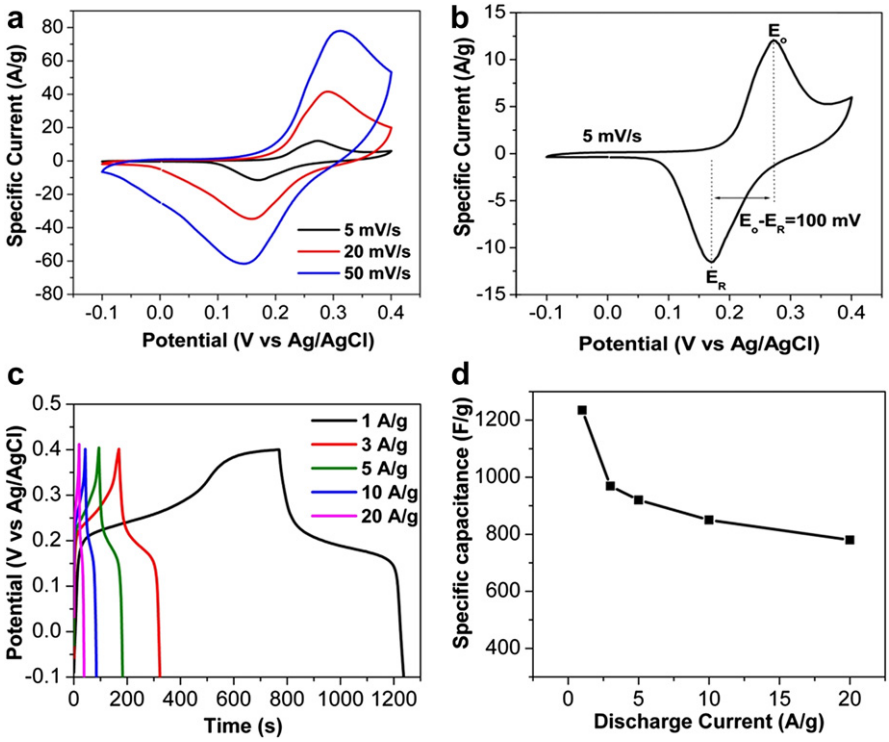

Fig. 3. Electrocapacitive properties of sample RGOCNT-15-4: (a) CV curves at various scan rates, (b) CV plot at a scan rate of 5 mV s^{-1}, (c) galvanostatic charge–discharge curves at different current densities, and (d) specific capacitance as a function of discharge current.

electrode mass. More importantly, the rate performance of the composite electrode (Fig. 3d) showed that the specific capacitance values were as high as 850 F g^{-1} and 780 F g^{-1} when the discharge rate increased to 10 A g^{-1} and 20 A g^{-1}, respectively, indicating a very promising electrode for high-energy and high-power supercapacitors. It should be noted that nickel hydroxide has a low operating potential window (~0.5 V). This drawback can be overcome by fabricating asymmetric electrochemical capacitors with nickel hydroxide as the positive electrode and carbon as the negative electrode.

To examine the effect of CNTs and nickel species on the performance of the RGOCNT composites, electrochemical measurements were carried out on another two samples with longer CNTs (RGOCNT-30-2) and less nickel content (RGOCNT-15-0.6). Their CV curves are shown in Fig. S3 and the electrochemical properties are compared with pure RGO sample and commercial multi-walled CNTs (MWCNTs) in Table 1.

The CV curves (Fig. S3) for both RGOCNT-15-0.6 and RGOCNT-30-2 electrodes showed one pair of reversible redox peaks (one anodic and one cathodic peak), similar to that of sample RGOCNT-15-4, indicating highly reversible electrode reaction between Ni (II) and Ni (III). The small value of ΔE_{OR} and large potential difference between E_{OE} and E_O shown in Table 1 provide additional support on the redox reaction. However, other characteristics of the three composite electrodes are different. Comparing the CV curves of RGOCNT-15-0.6 (Fig. S3a) with that of RGOCNT-15-4 (Fig. 3a), a lower specific current was obtained from the former. When RGOCNT-30-2 with longer CNTs was used as electrode, a lower specific current was seen (Fig. S3b). This is an indication of the inferior capacitive performance of RGOCNT-30-2 than that of RGOCNT-15-4 and RGOCNT-15-0.6.

Fig. 4 shows the average specific capacitance against discharge current for different electrode materials. It is seen that both RGOCNT-15-4 and RGOCNT-15-0.6 outperformed other electrode materials. The best capacitive performance was observed from electrode $Ni(OH)_2$-embedded-RGOCNT-15-4 in the whole current density range. While RGOCNT-30-2 showed an inferior performance, its specific capacitance value was two-fold higher than that

Table 1
Electrochemical characteristics of various electrode materials.

Samples	1 (A g^{-1})	3 (A g^{-1})	5 (A g^{-1})	10 (A g^{-1})	20 (A g^{-1})	E_O-E_R (mV)	$E_{OE}-E_O$ (mV)
RGOCNT-15-4	1235	969	920	850	780	100	130
RGOCNT-15-0.6	385	344	309	268	220	100	144
RGOCNT-30-2	43	41	39	40	36	83	138
RGO	88	78	76	73	69	–	–
MWCNT	21	20	20	20	20	–	–

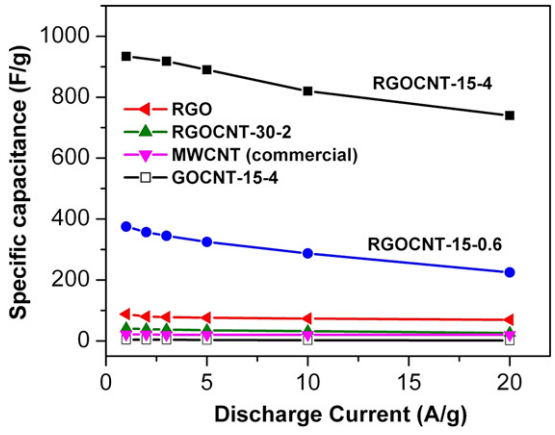

Fig. 4. Specific capacitance again discharge current for various electrode materials.

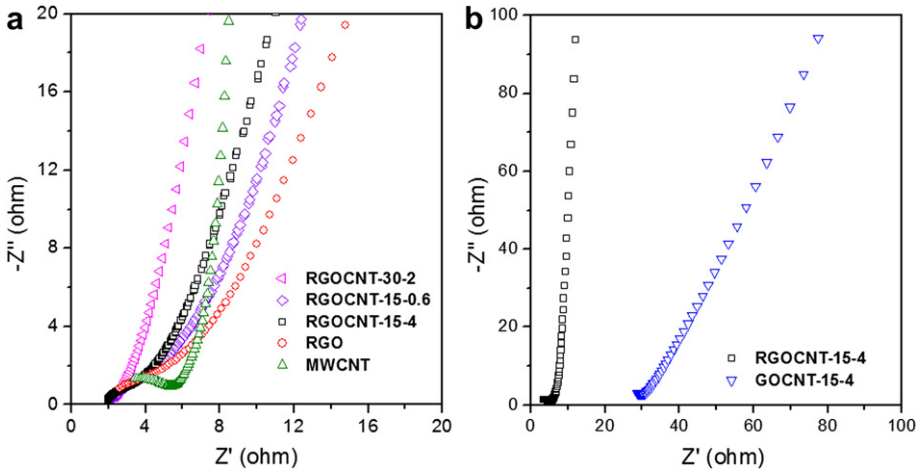

Fig. 5. Nyquist plots of (a) different electrode materials, and (b) samples RGOCNT-15-4 and GOCNT-15-4.

of the commercial MWCNTs with good rate performance. In the present work, pure GO was also used as the substrate to grow CNTs to prepare GOCNT-15-4 composite under similar experimental conditions as that of RGOCNT-15-4. In strong contrast to the $Ni(OH)_2$-embedded-RGOCNT-15-4, sample GOCNT-15-4 showed a significantly inferior electrochemical performance with a specific capacitance value less than 5 F g^{-1} as seen from Fig. 4. Such a remarkable difference in capacitive performance of the composite electrodes arose from their different physical and chemical properties.

The electrochemical impedance spectroscopy (EIS) technique was employed to assess the electrochemical frequency behavior of various electrode materials in an alkaline solution. The EIS data were analyzed using Nyquist plots and are presented in Fig. 5. It is clearly seen from Fig. 5a that all RGOCNT composites displayed a better ionic transport behavior than that of the pure RGO electrode and the commercial MWCNT electrode as evidenced by the negligible high frequency resistor–capacitor (RC) loops or semicircles and the smaller Warburg region for the RGOCNT electrodes [24,25,38]. The total resistance obtained from the Nyquist plots was in the order of RGOCNT-30-2 (1.7 Ω) < RGOCNT-15-4 (2 Ω) < RGOCNT-15-0.6 (2.3 Ω) < RGO (2.8 Ω) < commercial MWCNTs (4.5 Ω). On sharp contrast, a very strong ion diffusion resistance was obtained from GOCNT-15-4, which had a total resistance of 30 Ω.

Room temperature electrical conductivity was measured using the two-probe method [28,29]. It was found that after pillaring RGO platelets with CNTs, the electrical conductivity was increased from 277 S m^{-1} to 457 S m^{-1}. Therefore, both the EIS and the electrical conductivity data confirmed that the RGOCNT composites possessed a very good electric conductivity, which is favorable for applications requiring fast electron and ionic transportation.

Table S1 summarizes the porous properties and the chemical compositions of the samples. It is seen that sample RGOCNT-30-2 had the lowest specific surface area of 26 m^2 g^{-1}, similar to that of the commercial MWCNTs. The other two RGOCNT composites with shorter CNTs both had a higher specific surface area (350 m^2 g^{-1} for RGOCNT-15-4 and 307 m^2 g^{-1} for RGOCNT-15-0.6). In addition, based on the XPS analysis, the mass content of nickel was found to be 21.7 wt%, 7.6 wt% and 4.3 wt% for samples RGOCNT-15-4, RGOCNT-15-0.6 and RGOCNT-30-2, respectively. With the similar specific surface area of samples RGOCNT-15-4 and RGOCNT-15-0.6, nearly three times more nickel content in the former led to largely enhanced capacitance value than the later. While RGOCNT-30-2 showed a similar porosity with that of the commercial MWCNTs, the slightly larger capacitance value was probably due to the pseudocapacitance of the nickel hydroxide.

The intimate contact between the nickel hydroxide with the carbon nanotube is another important and unique characteristic of the 3D nanostructures described in this paper. As the nickel nanoparticles were semi-embedded into the CNTs in the composite structure, the wall of the CNT can 'hold' the Ni species firmly during the electrochemical reaction. On the other hand, the active material was highly accessible and the size of the Ni nanoparticles (30–40 nm) was just appropriate for the efficient utilization of their pseudoproperties [15]. Indeed, the electrochemical stability test (Fig. 6) showed that composite electrode RGOCNT-15-4 retained 80% of its original capacitance after 500 cycles at a very high discharge current density of 10 A g^{-1}, indicating a good cycle ability of the composite electrode.

Table 2 compares some important electrocapacitive characteristics (obtained under similar characterization conditions) of various psedudocapacitor electrode materials reported in the literature with that of the composite materials prepared in this work. The advantages of our materials in terms of specific capacitance, rate capability and cycle stability are clearly seen, indicating the composite materials are potential electrode for high-performance supercapacitor application.

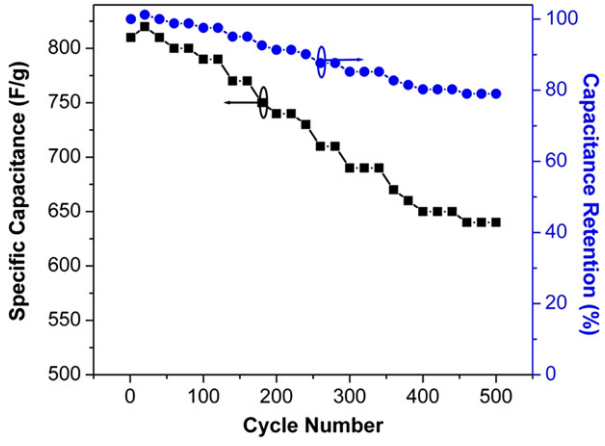

Fig. 6. Cycling performance of sample RGOCNT-15-4 at a discharge current density of 10 A g^{-1}.

Table 2
A comparison of various pseudocapacitor electrodes.

Materials	Preparation method	Electrical conductivity ($S\ m^{-1}$)	Specific capacitance ($F\ g^{-1}$)[a]	Specific capacitance at the highest current density ($F\ g^{-1}$)[b]	Cycle stability
$Ni(OH)_2$-RGOCNT (this work)	CVD + electrochemical conversion	457	1235 F g^{-1} at 1 A g^{-1}	780 F g^{-1} at 20 A g^{-1}	80% Capacity retained after 500 cycles at 10 A g^{-1}
$Ni(OH)_2$-GS [8]	Hydrolysis + hydrothermal treatment	Not reported	935 F g^{-1} at 2.8 A g^{-1}	667 F g^{-1} at 45 A g^{-1}	No obvious capacity loss after 2000 cycles at 28 A g^{-1}
$Ni(OH)_2$-Ni foam [9]	Electrodeposition	Not reported	3152 F g^{-1} at 4 A g^{-1}	280 F g^{-1} at 16 A g^{-1}	52% Capacity retained after 300 cycles at 4 A g^{-1}
$Ni(OH)_2$-AC [18]	Chemical precipitation	Not reported	314 F g^{-1} at 2 mV s^{-1}	Not evaluated	85% Capacity retained after 350 cycles at 0.04 A g^{-1}
Porous NiO film [39]	Chemical bath deposition + template removal	Not reported	309 F g^{-1} at 1 A g^{-1}	221 F g^{-1} at 40 A g^{-1}	89% Capacity retained after 4000 cycles at 1 A g^{-1}
β-$Ni(OH)_2$ film [7]	Chemical bath deposition	Not reported	398 F g^{-1} at 5 mV s^{-1}	92 F g^{-1} at 150 mV s^{-1}	Not evaluated
$Ni(OH)_2$ nanoflakes [15]	Hydrothermal treatment	Not reported	1715 F g^{-1} at 5 mV s^{-1}	574 F g^{-1} at 100 mV s^{-1}	78% Capacity retained after 2000 cycles at 50 mV s^{-1}

[a] The specific capacitance was all measurement under similar experimental condition with a three-electrode cell configuration.
[b] The specific capacitance measured at the highest current density in the respective literature report.

4. Conclusions

In summary, we have demonstrated the preparation of 3D $Ni(OH)_2$-embedded-RGOCNT composite materials with excellent electrocapacitive properties. The symmetric supercapacitor based on electrode RGOCNT-15-4 exhibited a high specific capacitance (1235 F g^{-1} at a current density of 1 A g^{-1}) with an excellent rate capability and a good cycle stability. The unique advantages of such 3D nanostructures as a supercapacitor electrode include fast ion and electron transfer throughout the electrode matrix, highly accessible pseudoactive materials with efficient utilization, excellent reversible redox reactions of the nickel hydroxide nanoparticles and the strong interaction between the carbon matrix and the pseudoactive material. We have also shown that the use of a conducting substrate (RGO), the morphology of the carbon nanotube and the amount of nickel particles strongly affect the electrochemical performance of the composite materials. Considering the excellent capacitive performance of the $Ni(OH)_2$ embedded-RGOCNT composite material, coupling this new carbon material with a suitable counter electrode to fabricate asymmetric capacitors may boost the electrocapacitive performance.

Acknowledgments

Financial support from The Australian Research Council (ARC) under the ARC Future Fellow Program (FT100100879) is acknowledged.

Appendix A. Supporting information

Supporting information related to this article can be found at http://dx.doi.org/10.1016/j.jpowsour.2012.09.016.

References

[1] D. Linden, Handbook of Batteries, McGraw-Hill, New York, 2002.
[2] J. McBreen, Modern Aspects of Electrochemistry, vol. 21, Plenum, New York, 1990.
[3] M.S. Wu, C.M. Huang, Y.Y. Wang, C.C. Wan, Electrochim. Acta 44 (1999) 4007–4016.
[4] T.N. Ramesh, R.S. Jayashree, P.V. Kamath, S. Rodrigues, A.K. Shukla, J. Power Sources 104 (2002) 295–298.
[5] W.K. Hu, D. Noreus, Chem. Mater. 15 (2003) 974–978.
[6] D.D. Zhao, W.J. Zhou, H.L. Li, Chem. Mater. 19 (2007) 3882. 3791.
[7] U.M. Patil, K.V. Gurav, V.J. Fulari, C.D. Lokhande, O.S. Joo, J. Power Sources 188 (2009) 338–342.
[8] H.L. Wang, H.S. Casalongue, Y.Y. Liang, H.J. Dai, J. Am. Chem. Soc. 132 (2010) 7472–7477.
[9] G.-W. Yang, C.L. Xu, H.L. Li, Chem. Commun. (2008) 6537. 6359.
[10] F.S. Cai, G.Y. Zhang, J. Chen, X.L. Gou, H.K. Liu, S.X. Dou, Angew. Chem. Int. Ed. 43 (2004) 4212–4216.
[11] D. Singh, J. Electrochem. Soc. 145 (1998) 116–120.
[12] J. Chen, D.H. Bradhurst, S.X. Dou, H.K. Liu, J. Electrochem. Soc. 146 (1999) 3606–3612.
[13] K. Matsui, T. Kyotani, A. Tomita, Adv. Mater. 14 (2002) 1216–1219.
[14] Z.H. Liang, Y.J. Zhu, X.L. Hu, J. Phys. Chem. B 108 (2004) 3488–3491.
[15] H. Jiang, T. Zhao, C.Z. Li, J. Ma, J. Mater. Chem. 21 (2011) 3818–3823.
[16] A. Sierczynska, K. Lota, G. Lota, J. Power Sources 195 (2010) 7511–7516.
[17] Q.D. Wu, X.P. Gao, G.R. Li, G.L. Pan, T.Y. Yan, H.Y. Zhu, J. Phys. Chem. C 111 (2007) 17082–17087.
[18] Q. Huang, X. Wang, J. Li, C. Dai, S. Gamboa, P.J. Sebastian, J. Power Sources 164 (2007) 425–429.
[19] H.L. Wang, J.T. Robinson, G. Diankov, H.J. Dai, J. Am. Chem. Soc. 132 (2010) 3270–3271.
[20] G.K. Dimitrakakis, E. Tylianakis, G.E. Froudakis, Nano Lett. 8 (2008) 3166–3170.
[21] Z.J. Fan, J. Yan, L.J. Zhi, Q. Zhang, T. Wei, J. Feng, M.L. Zhang, W.Z. Qian, F. Wei, Adv. Mater. 22 (2010) 3723–3728.
[22] L.L. Zhang, S. Li, J. Zhang, P. Guo, J. Zheng, X.S. Zhao, Chem. Mater. 22 (2010) 1195–1202.
[23] D.H. Wang, R. Kou, D. Choi, Z.G. Yang, Z.M. Nie, J. Li, L.V. Saraf, D.H. Hu, J.G. Zhang, G.L. Graff, J. Liu, M.A. Pope, I.A. Aksay, ACS Nano 4 (2010) 1587–1595.
[24] L.L. Zhang, S.Y. Zhao, X.N. Tian, X.S. Zhao, Langmuir 26 (2010) 17624–17628.
[25] K. Zhang, L.L. Zhang, X.S. Zhao, J. Wu, Chem. Mater. 22 (2010) 1392–1401.
[26] L.L. Zhang, Z.G. Xiong, X.S. Zhao, ACS Nano 4 (2010) 7030–7036.
[27] W.S. Hummers, R.E. Offeman, J. Am. Chem. Soc. 80 (1958) 1339.
[28] F. Su, X.S. Zhao, Y. Wang, J.Y. Lee, Microporous Mesoporous Mater. 98 (2007) 323–329.
[29] Z.B. Lei, Z.W. Chen, X.S. Zhao, J. Phys. Chem. C 114 (2010) 19867–19874.
[30] M. Seredych, D. Hulicova-Jurcakova, G.Q. Lu, T.J. Bandosz, Carbon 46 (2008) 1475–1488.
[31] D. Hulicova, M. Kodama, H. Hatori, Chem. Mater. 18 (2006) 2318–2326.
[32] K. Otsuka, Y. Abe, N. Kanai, Y. Kobayashi, S. Takenaka, E. Tanabe, Carbon 42 (2004) 727–736.
[33] R.S.S. Guzman, J.R. Vilche, A.J. Arvia, J. Electrochem. Soc. 125 (1978) 1578–1587.
[34] A. Seghiouer, J. Chevalet, A. Barhoun, F. Lantelme, J. Electroanal. Chem. 442 (1998) 113–123.
[35] C.E. Dube, B. Workie, S.P. Kounaves, A. Robbat, M.L. Aksu, G. Davies, J. Electrochem. Soc. 142 (1995) 3357–3365.
[36] D.A. Corrigan, R.M. Bendert, J. Electrochem. Soc. 136 (1989) 723–728.
[37] W.H. Zhu, J.J. Ke, H.M. Yu, D.J. Zhang, J. Power Sources 56 (1995) 75–79.
[38] R. Kotz, M. Carlen, Electrochim. Acta 45 (2000) 2483–2498.
[39] X.H. Xia, J.P. Tu, X.L. Wang, C.D. Gu, X.B. Zhao, J. Mater. Chem. 21 (2011) 671–679.